Determination of the Three-Dimensional Structure of Ferrihydrite Nanoparticle Aggregates

5 AUTHORS, INCLUDING:

Benjamin Legg
Pacific Northwest National Laboratory
9 PUBLICATIONS **122** CITATIONS

SEE PROFILE

Mengqiang Zhu
Lawrence Berkeley National Laboratory
23 PUBLICATIONS **373** CITATIONS

SEE PROFILE

Luis R. Comolli
Lawrence Berkeley National Laboratory, Ber...
59 PUBLICATIONS **1,363** CITATIONS

SEE PROFILE

Langmuir

# Determination of the Three-Dimensional Structure of Ferrihydrite Nanoparticle Aggregates

Benjamin A. Legg,*,[†,∥] Mengqiang Zhu,[‡,⊥] Luis R. Comolli,[§] Benjamin Gilbert,[§] and Jillian F. Banfield[§]

[†]Earth and Planetary Science, University of California—Berkeley, Berkeley, California 94720, United States

[‡]Earth Science Division and [§]Life Sciences Division, Lawrence Berkeley National Laboratory, Berkeley, California 94720, United States

S Supporting Information

ABSTRACT: Aggregation impacts the reactivity, colloidal stability, and transport behavior of nanomaterials, yet methods to characterize basic structural features of aggregates are limited. Here, cryo-transmission electron microscope (cryo-TEM) based tomography is utilized as a method for directly imaging fragile aggregates of nanoparticles in aqueous suspension and an approach for extracting quantitative fractal dimensions from the resulting three-dimensional structural models is introduced. The structural quantification approach is based upon the mass autocorrelation function, and is directly comparable with small-angle X-ray scattering (SAXS) models. This enables accurate characterization of aggregate structure, even in suspensions where the aggregate cluster size is highly polydisperse and traditional SAXS modeling is not reliable. This technique is applied to study real suspensions of ferrihydrite nanoparticles. By comparing tomographic measurements with SAXS-based measurements, we infer that certain suspensions contain polydisperse aggregate size distributions. In other suspensions, fractal-type structures are identified with low intrinsic fractal dimensions. The fractal dimensions are lower than would be predicted by simple models of particle aggregation, and this low dimensionality enables large, low-density aggregates to exist in stable colloidal suspension.
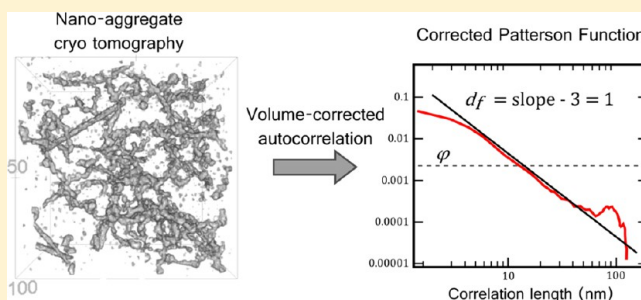
■ INTRODUCTION

The ability to accurately characterize nanoparticle aggregates is a pressing scientific need. Aggregation of nanoparticles impacts their reactivity, colloidal stability, transport behavior, and biological interaction with particles.[1−3]

Traditional methods for aggregate characterization are limited in their ability to resolve nanoscale structures in aqueous solution. Direct imaging methods, such as transmission electron microscopy (TEM), are traditionally performed on dried samples and are likely to destroy or alter fragile aggregate features. In the absence of direct structural images, scientists have historically relied on indirect methodologies such as small-angle X-ray scattering (SAXS) to characterize nanoparticle aggregates. SAXS provides quantitative structural data, but interpretation requires an accurate a priori understanding of the relevant structural features, since it is often possible to fit a SAXS pattern equally well by using substantially different physical models. Methods for confirming these models are therefore vitally important.

Recently, cryogenic transmission electron microscopy (cryo-TEM)[4] has been introduced as a method for direct in aqua imaging of nanoparticles[5] and nanoparticle aggregates.[6] This method utilizes rapid quenching to produce thin films of vitreous ice, preserving the nanoparticle aggregate intact for observation in the TEM. The aggregate structure can then be determined directly and unambiguously, in aqua. Cryogenic electron tomography[7] (cryo-ET) is an extension of cryo-TEM that has been used to produce full, three-dimensional representations of nanoscale aggregates.[8,9] As we will demonstrate, cryo-ET and SAXS are highly complementary methods, with cryo-ET helping to inform SAXS interpretation. In this work, cryo-ET provides insights into the validity of the structural models that underlie traditional SAXS analysis.

In this work we seek to determine the aggregate structure of real nanoparticle aggregates. We chose to study synthetic ferrihydrite nanoparticles, as an interesting and environmentally important test case for this relatively new method. Ferrihydrite is a commonly occurring ferric oxyhydroxide mineral that is known to form a variety of complex colloidal structures, including stable particle aggregates.[10,11] The aggregate structure of ferrihydrite is important to understand, because it is believed to impact its environmental transport properties, geochemical reactivity, and bioavailability.

We focus on quantifying the aggregate's structural fractal dimension, since this is known to have important ramifications for aggregate behavior (e.g., sedimentation, mechanical strength, and gelation),[12,13] and can also provide insights into the aggregation mechanism.[14] Cryo-ET allows us to establish that

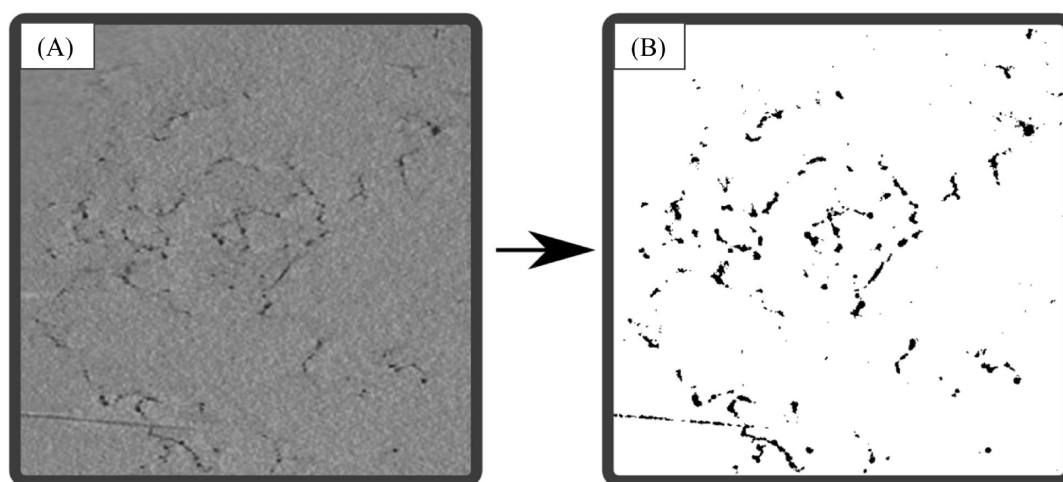A   dx.doi.org/10.1021/la502128d | Langmuir XXXX, XXX, XXX–XXX

Figure 1. Example of two-dimensional slice from a cryo-TEM tomogram. (A) Cross-section from an original tomographic reconstruction. Dark regions inidcate ferrihydrite particles. (B) Corresponding segmented cross-section. Three-dimensional structural models are constructed by segmenting each tomogram slice.

ferrihydrite aggregates can form branched fractal networks with a remarkably linear structure and with a fractal dimension that is quantitatively lower than would be typically expected from simple growth models. The environmental consequences of such structures will be investigated more in a later paper.

By pairing cryo-ET with SAXS, we are able to explore the strengths and weaknesses of each method. Although cryo-ET has inherently lower sampling statistics than SAXS, it is possible to obtain certain aggregate properties (such as fractal dimension and particle size) that would traditionally be obtained by SAXS. We can subsequently incorporate these results into an appropriate SAXS model and interpret SAXS data more reliably. Our analysis indicates that aggregate size polydispersity can have an important influence on the SAXS pattern of real aggregates and this could lead to the misinterpretation of SAXS data if the patterns are evaluated using more common assumptions about aggregate structure.

■ EXPERIMENT

Particle Synthesis. Suspension (35 mL each) of iron oxy-hydroxide nanoparticles were formed via microwave flash precipitation from ferric nitrate, as described by Guyodo et al.[11] Final ionic strength was adjusted by dialysis against 18 MΩ water, to a final conductivity of <200 μS/cm and pH of approximately 4.5 (note that suspension was not buffered). X-ray diffraction confirms a six-line ferrihydrite phase. Precipitate mass fraction is ∼3.5 mg/mL. When stored at 4 °C, these suspensions are stable against flocculation and aggregate reconstruction for several months. Nanoparticles were prepared in multiple batches so as to generate sufficient material for all analyses. Batches Syn10 and Syn15 were used for SAXS and TEM analysis.

Syn10 was stored at 4 °C for approximately 1 year prior to analysis whereas Syn15 was characterized soon after synthesis. Because initial characterization of Syn15 showed qualitatively different features than Syn10, Syn15 was reanalyzed with SAXS and cryo-TEM after storage at 4 °C for 1 month and 8 months, to investigate the possibility of reconstruction over time. Three subsamples of Syn15 were also taken immediately after synthesis, then aged for 10 days at 4, 35, and 55 °C, respectively, to assess the impact of temperature on aggregate reconstruction. Prior to analysis, all samples were diluted to appropriate concentrations for SAXS and TEM by adding 150 μL into 18 MΩ water to reach a final volume of 1.5 mL. This method also enabled complementary experiments where solution chemistry is controlled (not included in this study). SAXS experiments at different dilution factors show that dilution with deionized water does not significantly impact the aggregate structure.

Cryo-TEM. Cryo-TEM samples were prepared by applying a 2−μL drop of diluted ferrihydrite suspension onto a carbon-coated lacey Formvar TEM grid (Ted-Pella, P.N. 881F). Prior to application, grids were made hydrophilic by plasma discharge and rinsed with a 2 mM NaNO$_3$ solution to optimize sample−grid interactions. For tomographic data sets, 1 μL of 10 nm citrate capped gold colloid (BBInternational) was preapplied to the grid and allowed to dry before sample application; these particles serve as fiducial markers for image registration.

Excess suspension was removed by blotting with cellulose filter paper, to leave a thin film (∼100−300 nm thick) of suspension on the lacey grid. The grid was plunged into liquid ethane at −180 °C, quenching rapidly enough to produce a vitreous (glassy) ice with the aggregate structure preserved intact. The vitreous ice is electron transparent, allowing the aggregate structure to be imaged directly in TEM using a cryochilled stage, held at −180 °C with liquid nitrogen.

Cryo-TEM is performed using 200 keV Phillips CM200, and a JEOL JEM-3100FFC, operated at 300 keV, with an in-column Omega energy filter at Lawrence Berkeley National Laboratory. In addition to traditional two-dimensional (2D) images, five tomographic reconstructions were acquired using the JEOL 3100. These reconstructed volumes contained extended aggregates, frozen intact within a film of ice. Each tomographic data set consists of 65−70 images, acquired at 2° intervals, with maximum tilt angle of ±70° (single tilt axis). Three data sets were obtained of Syn10, with 0.54 nm pixel (voxel) size, and two of Syn15, with 0.22 nm pixel (voxel) size. Image contrast was produced by a combination of incoherent scattering and phase contrast imaging, with optimal defocus between 500 and 2000 nm.

Tomographic Reconstruction. Tomographic tilt series were aligned by gold fiducial tracking in the IMOD software package,[15] and reconstruction of the 3D volume was performed using the SIRT backprojection algorithm in tomo3D.[16] The resulting tomogram has a size of 1024 × 1024 × 512 voxels or 2056 × 2056 × 512 voxels. The computed 3D volume is then segmented to distinguish particle from the ice background. The automated trainable segmentation algorithm in FIJI[17] was used; it provided superior results when compared with segmentation approaches based on intensity thresholding of a bilateral filtered volume. After segmentation, the binary image was cleaned using a 3D erosion and dilation filter sequence (an opening filter). This produces a three-dimensional aggregate model from which physical properties can be computed. An example of the segmentation is provided in Figure 1. Upon careful examination, it can be seen that particle size is not completely preserved.

Small-Angle X-ray Scattering. SAXS analysis of aqueous suspensions was performed at ALS beamline 7.3.3, Lawrence Berkeley
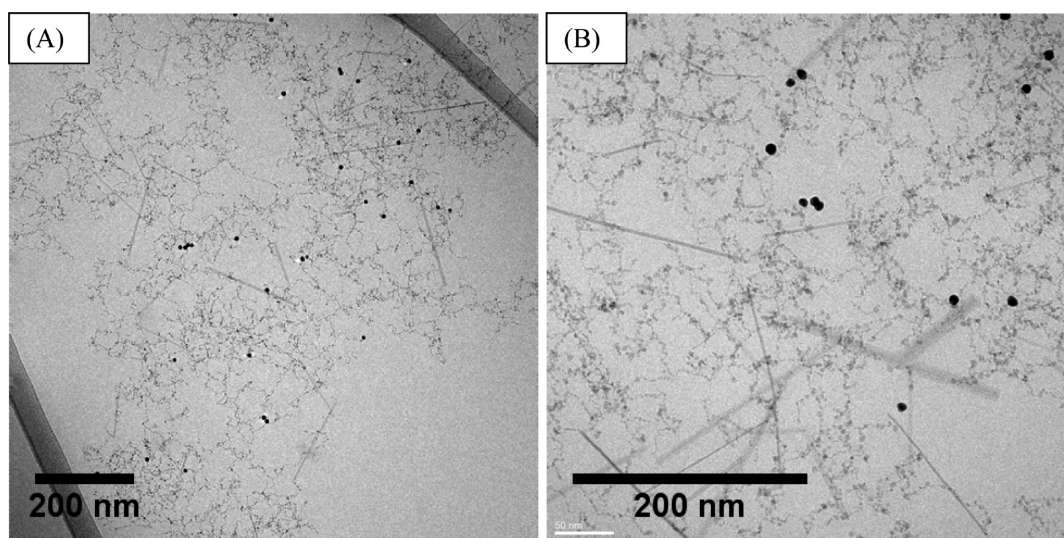
Figure 2. Representative cryo-TEM images of Syn10 in dionized water. (A) 50 kX, JEOL 3100 image. (B) 120 kX, JEOL3100 image. Both images show extended nanoparticle aggregates. The linear-branched particle chain structure is apparent, with a very limited amount of collapse into denser clumps. During aging, some fraction of particles have transformed into rods (∼200 nm long). High-contrast (dark) spherical particles are gold fiducial nanoparticles. The carbon-coated formvar support is visible in A in the upper right and lower left corners. There is some degree of mottling visible on the ice surface, but general transparency and lack of strong diffraction contrast indicates that the bulk of the ice in these samples is vitreous.
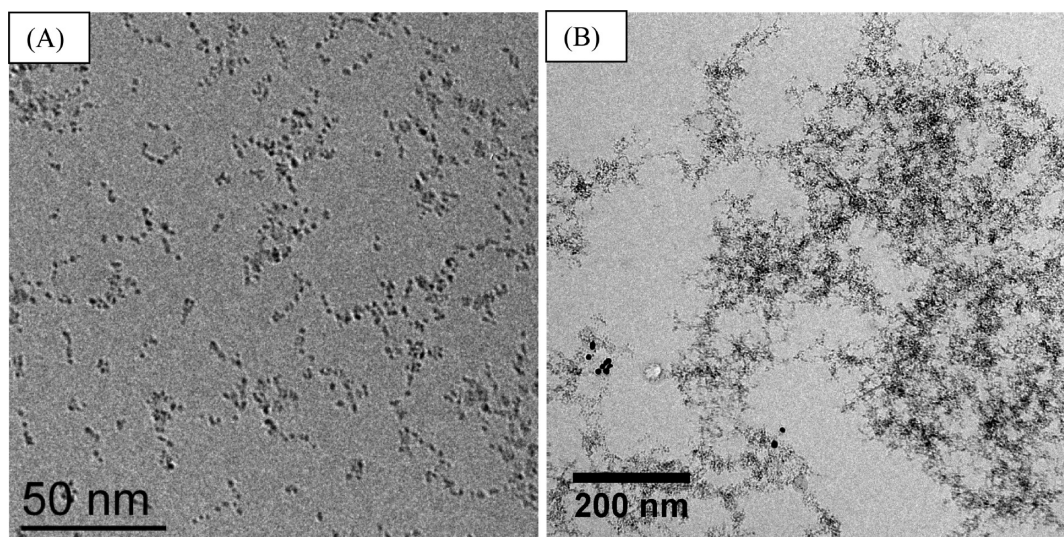

Figure 3. (A) Cryo-TEM images from Syn15 in deionized water. The image is taken at 115 kX, CM200. Primary particles (3−5 nm diameter) are observed to cluster into small aggregates. The chainlike nature of particle clusters can be observed. Most aggregates are of limited extent and may range from just a few particles, to many thousands of particles. (B) Image taken at 60 kX, JEOL 3100. This shows a large Syn15 aggregate. The aggregates in Syn15 samples generally appear to be more densly packed than those seen in Syn10.

National Laboratory, over a scattering q-range of 0.08−4 nm^{-1}. The scattering vector is defined relative to the 2θ scattering angle and X-ray wavelength as $q = 4\pi \sin(\theta)/\lambda$. Scattering was performed in transmission mode, with sample thickness of 1−2 mm and X-ray wavelength of 0.124 nm. Scattering patterns were acquired on a Pilatus 1 M CCD. Scattering angle was calibrated with a silver behenate reference, and deionized water reference solutions were characterized for background subtraction.

SAXS data were processed into 1D radial curves using the IRENA software package.[18] These 1-D curves were fit to analytical models using an iterative least-squares fitting approach. The models, described in greater detail in Theory and Calculations, considered the influence of primary particle radius, particle size distribution, aggregate fractal dimension, and aggregate cluster size.

■ RESULTS

Cryo-TEM. Cryo-TEM analysis of ferrihydrite suspensions revealed branched aggregate structures, composed of roughly spheroidal primary particles (Figure 2). The size distribution of primary particles was evaluated by manually counting particles in high-magnification TEM images (≥150,000×). Syn10 possessed a number-weighted mean radius, R_p = 1.25 nm, with a standard deviation in particle size ΔR_p = 0.31 nm (based on 320 particles), while, for Syn15, R_p = 1.31 nm and ΔR_p = 0.55 nm (based on 385 particles). Some micrographs recorded for Syn15 indicate a bimodal primary particle size distribution.

Syn10, shown in Figure 2, was aged at 4 °C for 1 year prior to analysis. Particles are arranged into a network of branched, linear chains. Approximately 10% of the sample (by volume)
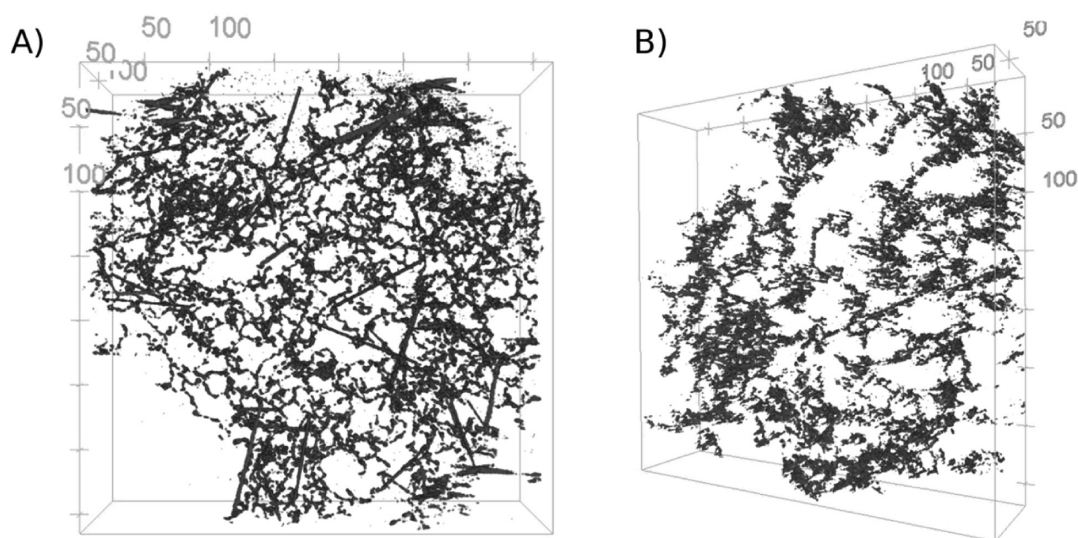
Figure 4. Two different tomographic reconstructions, both spanning volumes of 370 nm × 370 nm × 90 nm: (A) Syn10, particle volume fraction is ~2.2%; (B) reconstruction of Syn15, particle volume fraction is ~1.3%. Although both samples display a fractal-type structure, Syn15 has a greater tendency toward particle clustering to form course structures, while the particles in Syn10 tend to form more linear chains that are more evenly distributed throughout the aggregate.

consisted of lathlike particles. Previous studies using the same synthesis have identified rods similar to goethite,[19] but the identity here is uncertain, as no diagnostic goethite peaks were detectable in X-ray diffraction patterns (data not shown). The suspension was highly aggregated: most of the sample consisted of micrometer-scale aggregates, but the aggregates show an open structure with fairly low density of particles and significant open space.

Syn15 cryo-TEM samples also contained fractal aggregates, but with a different structure from those in Syn10. None of the Syn15 samples contained lathlike particles, even after thermal aging. Samples prepared 12 days after synthesis showed very high polydispersity of aggregate sizes, ranging from just a few particles across to micrometer scale (see Figure 3A). The linear motif seen in Syn10 is less obvious in Syn15; dense clusters of particles seem more prevalent. Subbatches of Syn15 aged at different temperatures were indistinguishable from each other. Samples of Syn15 prepared after storage for 8 months were structurally similar to those prepared after 12 days, but the aggregate cluster size was larger (smaller clusters were uncommon; Figure 3B). Rarely, large aggregates that have very high particle densities are found.

Tomographic Reconstructions. Three cryo-ET volumes were characterized that correspond to Syn10, and two tomographic volumes were prepared that correspond to Syn15. Volumes of 370 nm × 370 nm × 90 nm are extracted from two different tomograms and shown in Figure 4. Distinct differences can be seen between the two samples in terms of primary particle shape and aggregate structure. The reconstruction of Syn10 shows linear particle chains and displays lath-shaped particles that are not present in any Syn15 samples. Syn15 appears to be more coarsely aggregated, with particles localized in denser clusters.

In most tomographic volumes, the ice thickness is between 100 and 200 nm. However, in some of the Syn10 reconstructions (volume 2), ice is less than 100 nm thick, and the aggregate shows signs of reconstruction due to confinement. This is apparent due to a high density of particles

sitting at the surface of the ice. See the Supporting Information for additional perspectives of the tomographic volumes.

SAXS Results. In addition to the cryo-TEM analyses of samples described above, Syn10 and the suite of Syn15 samples were characterized by SAXS. Representative 1D SAXS curves, $I(q)$, are shown in Figure 5. An apparent fractal power-law regime can be observed for values of $q < {\sim}0.6$ nm^{-1}. At higher q values ($q > 2$ nm^{-1}), the Porod regime is observed, in which $I(q) \sim q^{-4}$ (however, uncertainties in the background subtraction have greatest impact at high-q values, which may lead to deviations from Porod behavior). Where $1/q$ is much greater than the aggregate size, a low-q plateau should be
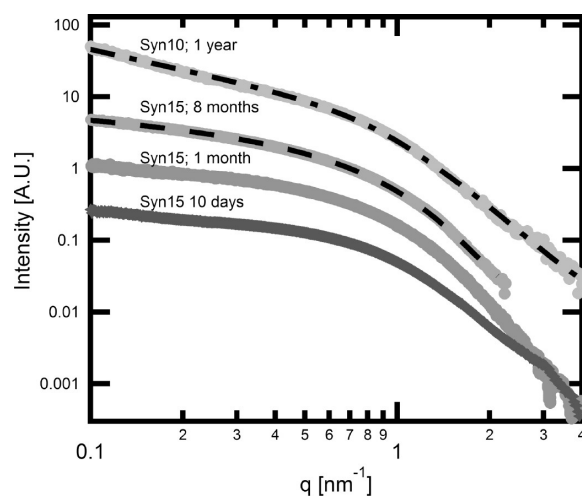

Figure 5. SAXS intensity profiles for Syn10 and Syn15 at different aging times. The fractal power-law regime is observed for q values of 0.6 nm^{-1} and less, and the Porod regime becomes evident for $q > 2$ nm^{-1}. Dashed lines represent best fits with analytical models. The model fit for Syn10 assumes a monodisperse array of aggregates, with $\xi = 400$ nm and with $d_f = 1.02$. Syn15 curves can only be fit by assuming polydisperse aggregate distributions. Here, an adequate fit can be obtained when $d_f = 1.59$ and the polydispersity exponent has a value of $\tau = 2$.

observed. Unfortunately, this plateau is not visible within the experimentally accessible q range, which means that SAXS measurements alone cannot be expected to fully constrain the aggregate cluster size distribution. The low-q slope of Syn10 is markedly steeper than all Syn15 samples, suggesting an *apparently* higher fractal dimension. Thermal aging and long-term storage have a very subtle influence on Syn15, only appearing to slightly smooth the low-q scattering signal. The data range for Syn15 at 8 months is truncated due a change in the SAXS beamline configuration.

These scattering curves were fit using a variation of the Teixeira fractal aggregate model.[20] This model describes $I(q)$ as a function of R_p (average primary particle radius), ΔR_p (primary particle size distribution breadth), d_f (mass fractal dimension), and ξ (cluster size parameter). The details of this fitting model will be discussed under Theory and Calculations.

SAXS fitting provides an estimate of R_p that is in good agreement with TEM measurements. For Syn10, R_p is estimated at 1.24 nm from SAXS. The primary particle size of Syn15 is estimated at 1.23 nm in freshly prepared samples, 1.65 nm after 1 month, and 1.81 nm after 8 months. This could be due to Ostwald ripening, or it could simply reflect an increase in the average particle coordination number (number of particle−particle contacts) over time, since both have a similar impact on the SAXS pattern. Estimates of fractal dimension are not reliable, because the values of ξ and d_f are inversely correlated, and this data set does not cover a wide enough q range to determine both independently. As a first fitting attempt, ξ was fixed at 400 nm (based on the observation that most aggregates are of this size or larger). With this parameter fixed, d_f for Syn10 was estimated to have a value of 1.02; this value is indicative of highly linear structures. Attempts to fit Syn15 with this approach were unsuccessful; the apparent value of d_f for all Syn15 samples ranged from 0.4 to 0.6. These very low apparent fractal dimensions of less than 1 are physically unrealistic. The most probable explanation for this discrepancy is that Syn15 possesses a wide range of aggregate sizes, including a significant population of smaller clusters. Such polydispersity can systematically affect the observed SAXS scattering curve, leading to apparent fractal dimensions that are lower than the true structural fractal dimension. This will be discussed further in Theory and Calculations. The Syn15 structure is also found to be fairly constant over time. Even after 8 months of aging, the low-q slope remains essentially unaltered.

■ THEORY AND CALCULATIONS

In this section, we present the methods by which the structural fractal dimension can be obtained from both SAXS and cryo-EM. There are various approaches for defining the fractal dimension, which are not all identical.[21,22] The fractal nature of aggregates was first recognized in terms of a scaling law between aggregate size and aggregate mass. Later, Sinha[23] and Teixeira[20] suggested on heuristic grounds that the mass autocorrelation function, $\mathbb{P}(\mathbf{r})$, for a fractal aggregate should display a power-law decay with an exponent that depends upon d_f.

$$\mathbb{P}(\mathbf{r}) \sim |\mathbf{r}|^{d_f - 3} \tag{1}$$

They demonstrated that the fractal dimension could be extracted from SAXS data, which is possible because the SAXS scattering pattern (i.e., differential scattering cross-section) is essentially a Fourier transform of the autocorrelation function (eq 2),

$$I(\mathbf{q}) = \int \mathbb{P}(\mathbf{r}) \, e^{-i\mathbf{q}\cdot\mathbf{r}} \, d\mathbf{r} \tag{2}$$

Since that time, the power-law decay of $\mathbb{P}(\mathbf{r})$ has become accepted by many researchers as the definitive property of fractal aggregates.[14,22] We refer to d_f as the structural fractal dimension. Its value is commonly estimated from a real-space image using simple box-counting algorithms, as implemented in a recent cryo-ET study on calcium phosphate.[8] Alternatively, one can calculate $\mathbb{P}(\mathbf{r})$ directly, as in the work of Meakin.[24] We choose to calculate $\mathbb{P}(\mathbf{r})$ directly, since this allows us to determine the fractal dimension while making use of the models and finite-size corrections that have been developed for SAXS-based approaches.

We emphasize that real aggregates do not possess the true scale invariance of a fractal. The branched fractal structure that we seek to characterize will only persist over a limited length scale, bounded by the size of the primary particles and the maximum extent of the aggregate. As we will show, the truncation of the fractal structure must be accounted for carefully.

Mathematical Representation of Aggregate Structure. This section establishes the mathematical framework for integrating SAXS with cryo-TEM. In either case, the full aggregate structure is represented by a three-dimensional density distribution function, $\rho(\mathbf{r})$. For simplicity, $\rho(\mathbf{r})$ is treated as a binary function with a value of $\Delta\rho$ when $\mathbf{r}$ lies within a particle and 0 if $\mathbf{r}$ lies in the solvent.

Neither experimental approach can fully provide $\rho(\mathbf{r})$. SAXS can only reveal the volume averaged properties of $\mathbb{P}(\mathbf{r})$, which is defined as $\mathbb{P}(\mathbf{r}) = \rho(\mathbf{r})\,\rho(-\mathbf{r})$. Conversely, the segmented cryo-TEM tomogram can provide a direct measurement of $\rho(\mathbf{r})$, but only over some finite volume. This finite volume truncation must be treated carefully if one wishes to obtain the fractal dimension. We represent the tomographic volume with the window function, $V_{tomo}(\mathbf{r})$. The tomographic image can then be represented mathematically as $\rho_{tomo}(\mathbf{r}) = V_{tomo}(\mathbf{r})\,\rho(\mathbf{r})$.

SAXS Modeling for Fractal Structures. The SAXS models developed by Sinha[23] and Teixera[20] recognized that $\mathbb{P}(\mathbf{r})$ can only follow the power-law relationship of eq 1 over a limited length scale. Rather than describe $\mathbb{P}(\mathbf{r})$ directly, Teixera posited eq 3 as an expression for the normalized particle pair-correlation function.

$$P(r) - 1 = \frac{D}{4\pi R_p^{d_f}} r^{d_f - 3} \exp\left(-\frac{r}{\xi}\right) \tag{3}$$

This expression is closely related to $\mathbb{P}(\mathbf{r})$; for aggregates of roughly spherical particles, $\mathbb{P}(\mathbf{r})$ can be obtained from $P(r)$, simply by a convolution with the particle shape function. Equation 3 possesses several important physical characteristics. At large distances, $P(r)$ converges to a constant value of 1. The corresponding behavior in $\mathbb{P}(r)$ is a convergence to $\Delta\rho^2\phi^2$, where ϕ represents the average volume fraction of the suspension. This is enforced by the exponential damping term, with a cutoff length of ξ, that is often taken as a measure of aggregate size. This behavior is in contradiction to ideal fractal behavior but must occur for real isotropic suspensions. The constant term does not contribute to observable SAXS intensity except at very small angles, but its presence is

important to note, because it means that traditional SAXS models assume that the power-law behavior of r^{d_f-3} is manifest with respect to the function $P(r) - 1$, or if one is dealing with the mass autocorrelation function, with respect to $\mathbb{P}(r) - \Delta\rho^2\phi^2$. It is therefore important to account for, if one intends to compare the fractal dimension obtained from a tomographic model with one obtained from SAXS-based measurements. If this subtraction is not considered, one can obtain significantly different results.

It should be noted that even eq 3 is only approximate. It fails, for example, to reflect the constraint that two particles cannot physically overlap. Fortunately, these corrections are less important if the system has some degree of primary particle polydispersity.[25,26] There is also considerable debate regarding the precise nature of the cutoff function for real aggregates; this will be addressed in greater detail in the next section.

From the particle pair-distribution function, Texiera determined an analytical solution for the scattering structure factor, $S(q)$. When combined with a model for the primary particle shape (in this study, we assume a Gaussian distribution of spheres with an averaged radius R_p and a distribution breadth ΔR_p), one can readily calculate a theoretical SAXS scattering pattern as a function of certain particle parameters (i.e., d_f, R_p, ΔR_p, and ξ). Experimentally obtained SAXS patterns can then be fit using iterative algorithms. We note that it is often possible to obtain good fits to $I(q)$ or $\mathbb{P}(r)$ while using an incorrect physical model. In the following section, we discuss how an ensemble of aggregates with different sizes may systematically bias SAXS estimates of fractal dimension. Cryo-ET is therefore an important independent check on SAXS-based results.

Treating Polydisperse Aggregates. The Teixeira aggregate model (eq 3) uses a simple, single-exponential damping term to account for the finite size of aggregate clusters. However, real suspensions may contain a polydisperse mixture of aggregate sizes. Teixeira,[20] Nicolai et al.,[27] and others have shown that aggregate size polydispersity can lead to apparent fractal dimensions that are lower than the true structural fractal dimension. This appears to be the case in Syn15, where cryo-TEM shows a wide range of aggregate cluster sizes, and SAXS fitting returned unphysically low apparent fractal dimensions of less than one.

For fractal aggregates, power-law size distributions are expected,[27,28] and the aggregate size distribution can be approximated as

$$N(n) \sim n^{-\tau} \exp(-n/n_c) \tag{4}$$

Here, n represents the number of particles in a cluster, and n_c is an aggregate cutoff size. As aggregation proceeds, n_c will grow.[29] The term τ describes the shape of the aggregate size distribution, with larger values of τ resulting in a higher proportion of small clusters. Its value has been correlated with aggregation mechanism, with DLCA resulting in $\tau \approx 0$ and RLCA resulting in $\tau \approx 1.5$ and, as the system approaches the percolation threshold, $\tau \approx 2.2$. According to the work of Nicolai, the depression of apparent fractal dimension is greatest for systems where n_c is small and τ is large.[27] In our study, Nicolai's approach is used to numerically generate synthetic SAXS profiles for an ensemble of aggregates.

It would be, in theory, possible to perform iterative fitting and obtain best-fit curves for the SAXS data as a function of d_f, R_p, ΔR_p, ξ, and τ. However, some of these values are highly correlated. Our SAXS data set is insufficient to constrain all five

of these variables as fitting parameters. Certain parameters (such as d_f) must be constrained by alternative methods (cryo-TEM).

Estimating the Autocorrelation Function from Tomographic Volumes. Tomographic imaging provides an avenue for estimating $\mathbb{P}(r)$ and calculating d_f that is independent of assumptions about aggregate size distribution. However, cryo-ET can generally only image a finite piece of some larger structure. Previous authors have outlined how the truncation of an infinite ideal aggregate to finite cluster size will systematically impact that object's autocorrelation function.[29,30] An analogous problem occurs when trying to estimate $\mathbb{P}(r)$, when only a small region of interest has been imaged. It is impossible to fully account for the missing information, but it is possible to remove the systematic truncation effects to obtain a better estimate for the intrinsic structural fractal dimension

In this study, an approach for removing the systematic truncation effects is developed based on the work of Yanwei and Meriani.[30] A homogeneous, infinitely large aggregate has an autocorrelation function of $\rho(\mathbf{r})\,\rho(-\mathbf{r})$. If just a small piece of that is isolated with tomography, it can be shown that the autocorrelation function for that fragment is

$$\rho_{tomo}(\mathbf{r})\,\rho_{tomo}(-\mathbf{r}) \approx [V_{tomo}(\mathbf{r})\,V_{tomo}(-\mathbf{r})][\rho(\mathbf{r})\,\rho(-\mathbf{r})] \tag{5}$$

Because $V_{tomo}(\mathbf{r})$ drops to zero beyond a certain regime, certain information is irretrievably lost during the application of eq 5. However, if one wishes to obtain an unbiased approximation to $\mathbb{P}(\mathbf{r})$, it is necessary to apply the following correction:

$$\mathbb{P}(\mathbf{r}) = \rho(\mathbf{r})\,\rho(-\mathbf{r}) \approx \frac{[\rho_{tomo}(\mathbf{r})\,\rho_{tomo}(-\mathbf{r})]}{[V_{tomo}(\mathbf{r})\,V_{tomo}(-\mathbf{r})]} \tag{6}$$

Aggregate inhomogeneity can also produce major systematic influences in a similar way. Although local inhomogeneity is inherent to fractal objects, when only a finite piece of a larger fractal is extracted, these local fluctuations can impede a direct assessment of the fractal dimension. Yanwei and Meriani identified this behavior in a mathematical analysis of theoretical aggregates, and similar behavior is seen to occur in these tomographic samples. Their work projects that eq 6 alone will often systematically overestimate $\rho(\mathbf{r})\,\rho(-\mathbf{r})$ at moderate distances (up to approximately half the width of V_{tomo}), and underestimate $\rho(\mathbf{r})\,\rho(-\mathbf{r})$ at higher distances. To correct for this, one must normalize $\rho_{tomo}(\mathbf{r})\,\rho_{tomo}(-r)$ by a factor that also accounts for particle density. The fully corrected autocorrelation function is estimated as follows:

$$\mathbb{P}(\mathbf{r}) = \rho(\mathbf{r})\,\rho(-\mathbf{r}) \approx \Delta\rho\phi\frac{(\rho_{tomo}(\mathbf{r})\,\rho_{tomo}(-\mathbf{r}))}{(\rho_{tomo}(\mathbf{r})\,V_{tomo}(-\mathbf{r}))} \tag{7}$$

Neither equation for estimating $\mathbb{P}(\mathbf{r})$ is entirely perfect. Based on analysis of real and synthetic aggregates, it is shown that eq 6 provides poor results when applied to sample volumes that are not homogeneously filled. In these cases, eq 7 does a better job of producing correlation functions which decay monotonically to a constant value, and the resulting subtracted curves, $\mathbb{P}(r) - \Delta\rho^2\phi^2$, tend to display a more idealized power-law regime. However, it can be argued that eq 7 is systematically ignoring certain long-range correlations that are inherent to the fractal structure; so for sample volumes that are

large and isotropic, the correlation functions produced by eq 6 may be more meaningful.

Analysis of Real and Simulated Tomographic Volumes. The following computational pipeline has been used to obtain an estimate of $\mathbb{P}(\mathbf{r})$ and calculate the fractal dimension for each tomographic volume.

Tomographic volumes were obtained using cryo-ET, focusing on individual, very large aggregates, because they can display the ideal r^{d_f-3} fractal behavior over the largest length scales. Volumes were segmented, down-sampled, and broken into subvolumes for processing. If the tomogram data did not completely fill a subvolume, a region of interest was defined, called V_{tomo}. However, only those subvolumes that were mostly spanned by the aggregate were used for further analysis.

The autocorrelations and cross-correlations for each subvolume were computed numerically, using zero-padded 3D FFT based algorithms in SciPy.[31] The resulting three-dimensional correlation functions are then spherically averaged and normalized (using both eq 6 and eq 7, for comparison), in order to estimate the ideal value for $\mathbb{P}(r)$.

For aggregates that mostly span their tomographic volume, $\mathbb{P}(r)$ estimated in this way converges toward a constant value of approximately $\Delta\rho^2\phi^2$ at large correlation lengths. This constant term is subtracted, and the power-law slope of $\mathbb{P}(r) - \Delta\rho^2\phi^2$ is measured. This correction is appropriate for treating fractal dimension of objects which have a short-range fractal order but that converge to a random isotropic behavior at longer correlation lengths (within the length scale of the sample volume).

These steps are shown graphically in Figure 6, for the computation of a single subvolume (from Syn 10, volume 1).
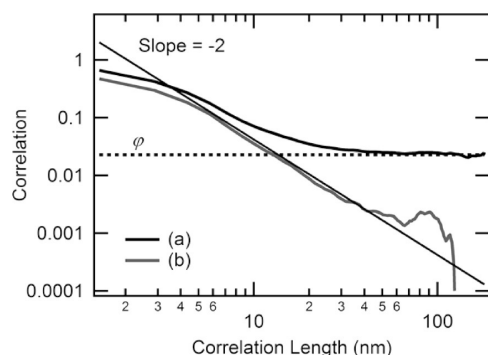
Figure 6. Curve a shows the estimated autocorrelation function, $\mathbb{P}(\mathbf{r})$, for a subvolume for Syn10 volume 1, as estimated by numerical computation and application of eq 7, and normalized by $\mathbb{P}(\mathbf{0})$. As expected, this curve now converges toward a constant value ϕ at large r. In curve b, the constant ϕ term has been subtracted to reveal the power-law decay. This particular volume has a slope of roughly -2, which corresponds to a fractal dimension of 1.

Curve a shows $\mathbb{P}(r)/\mathbb{P}(0)$, which has been obtained by application of eq 7. As expected, this converges toward a constant value of $\Delta\rho^2\phi^2/\Delta\rho^2\phi$ at large distances (within limits of statistical noise). Curve b shows the final, subtracted curves from which fractal dimension can be estimated. Note that if one measures the slope of $\mathbb{P}(r)$, instead of $\mathbb{P}(r) - \Delta\rho^2\phi^2$, a very different fractal dimension will be obtained. The fractal slope is only measured over a length scale between 5 and 55 nm; this range is selected such that r is greater than the primary particle diameter but less than some value where noise dominates the signal. To guide the eye, a line with slope of -2 (corresponding to a fractal dimension of 1; see eq 3) is shown in Figure 6. If the constant background were not subtracted, a larger estimate of the fractal dimension would be obtained. The fractal dimension for each aggregate is obtained by averaging the fractal dimension determined for each subvolume.

In order to determine whether the primary particle shape influences our estimate of fractal dimension, we have also performed the analysis on a "skeletonized" version of the aggregate structure (Figure 7, created in FIJI, with 3D erosion and skeletonization routines). The skeletonized structure should correspond more closely to $P(r)$, as opposed to $\mathbb{P}(\mathbf{r})$.

Estimates for d_f obtained by various methods are given in Table 1. The full tomographic structures typically show a slightly higher fractal dimension than their skeletonized counterparts, but the difference is small (suggesting that the measurement is fairly insensitive to particle shape, as hoped). For calibration, the method has been applied to the characterization of computationally generated DLA (distinct from DLCA) aggregates, which are expected to have fractal dimensions on the order of 2.5.[14] In these cases, the use of eq 6 shows better agreement with expected values than eq 7.

Dividing each sample into subvolumes prior to analysis allows the computation to be performed more rapidly (using $\sim$16 GB of memory). However, analyzing subvolumes also enables us to estimate the statistical reliability of our fractal dimension measurements and identify how specific physical properties of a subvolume might influence the measurement of fractal dimension.

For example, we find that eq 6 provides higher estimates of the fractal dimension than eq 7 when most of the aggregate's mass is located near the center of the tomographic subvolume, but a lower estimate if most of the aggregate mass is located near the edges of the tomographic subvolume.

We also found certain subvolumes (especially in Syn10 volume 2 and parts of Syn10 volume 3), in which confinement of the aggregates within a thin ice layer has caused a layer of particles to collect at the ice−vacuum interface (originally the water−air interface). This restructuring drives the measured fractal dimension trended toward larger values, approaching a value of 2 or more. This reflects the planar geometry of the particle accumulation. During the analysis of three tomographic volumes, the bulk of Syn10 appears to possess a very low intrinsic fractal dimension, somewhere between 1 and 1.4 (depending on measurement technique), but any given tomographic subvolume may possess an apparently larger fractal dimension if particles happened to accumulate at the surface. In particular, Syn10 volume 2 had significant surface reconstruction, and the fractal dimensions calculated from that tomogram should not be considered representative of the structure in bulk solution.

Compared with Syn10, Syn15 displays much higher fractal dimensions. This was somewhat surprising, since Syn15 had an apparently lower fractal dimension when measured with SAXS. However, in complex suspensions, a single fractal dimension is incapable of fully describing the aggregation state. Cryo-TEM methods show that, on the local scale, Syn15 clusters can be quite densely packed, but they also reveal that the suspension is a mixture of very large aggregates and many very small particle clusters. In this case, suspension polydispersity can explain the apparent discrepancies between SAXS-based and tomographic-
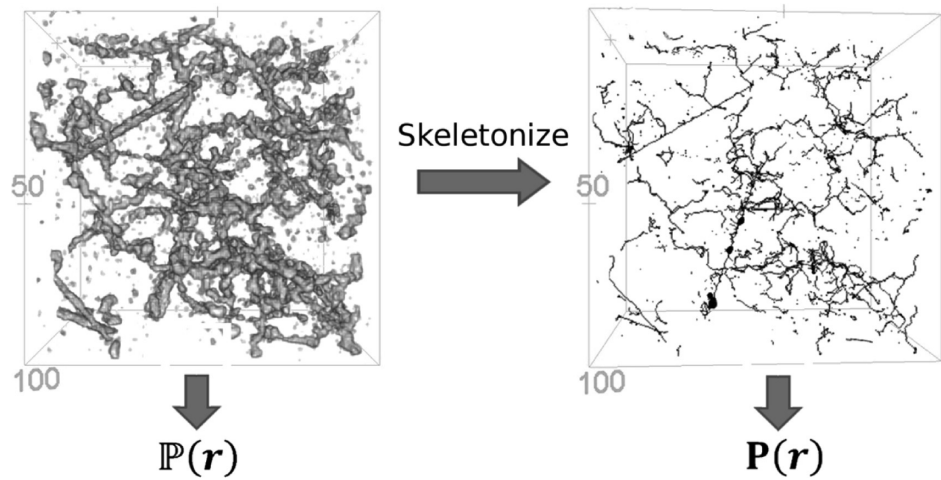
Figure 7. A $100 \times 100 \times 100$ nm tomographic volume, used for the estimation of $\mathbb{P}(\mathbf{r})$ and the corresponding aggregate skeleton, which can be used to obtain an estimate for the power-law dependence in $P(r)$, with less influence from particle shape.

Table 1. Estimates for $d_f{}^a$

	d_f				
	eq 6		eq 7		
sample		skeletonized		skeletonized	length scale probed
Syn15 vol 1	1.6 ± 0.1	1.5 ± 0.2	1.6 ± 0.1	1.5 ± 0.1	5−55 nm
Syn15 vol 2	1.9 ± 0.2	1.7 ± 0.2	1.7 ± 0.1	1.5 ± 0.3	5−50 nm
Syn10 vol 1	1.3 ± 0.1	1.2 ± 0.2	1.0 ± 0.2	1.0 ± 0.2	5−55 nm
Syn10 vol 2[b]	1.8 ± 0.2	1.8 ± 0.2	1.7 ± 0.2	1.7 ± 0.1	5−55 nm
Syn10 vol 3	1.4 ± 0.1	1.4 ± 0.1	1.3 ± 0.2	1.3 ± 0.2	5−55 nm
Synthetic DLA	2.2 ± 0.05	2.2 ± 0.05	2.0 ± 0.05	2.0 ± 0.05	2−20 rad

[a]Error designates estimated standard deviation of the mean. [b]These relatively high fractal dimension reflect aggregate reconstruction due to confinement within a thin film by ice surfaces.

based measurements of the fractal dimension. It is possible to fit the SAXS scattering profiles, using a fractal dimension of 1.5 or greater, if one supposes a polydisperse aggregate suspension where the cluster polydispersity exponent, τ, is between 2.0 and 2.2. One such fit has been shown in Figure 5.

■ DISCUSSION

Fractal Analysis. The application of fractal concepts to aggregates is common, but this work highlights the challenges involved in obtaining meaningful, quantitative measurements. For example, the aggregate structure of Syn15 would not have been apparent from SAXS analysis alone, since cluster polydispersity interferes with a dependable assessment of fractal dimension. The dramatic influence of polydispersity on the apparent fractal dimension is worth noting. Despite the fact that polydispersity effects were discussed in Teixeira's orignial paper,[20] most popular SAXS analysis packages such as NCNR SANS[33] or IRENA[18] do not currently implement polydispersity in their fractal analysis algorithms. Our work suggests that this structural feature should not be ignored for nanoscale aggregates.

In the process of this work, a second difficulty in performing SAXS experiments related to polydispersity was encountered. Very rarely, a Syn15 SAXS data set possessed anomalously large scattering in the low-q regime. This was initially regarded as an experimental error, as the signal typically disappeared upon repetition. However, based on our analysis that Syn15 consists of highly polydisperse aggregates, another explanation is

possible. The power-law cluster distributions described by eq 4 are "long tail distributions" in which a few very large clusters have the potential to dominate scattering. If such expressions truly hold for Syn15, then large statistical fluctuations in the amount of scattering from large aggregates are expected. The occasional inclusion of just one very large aggregate in the scattering volume could lead to the anomalous low-q scattering that was observed. It is in complex systems such as this where cryo-TEM provides a critical, localized viewpoint for describing the structures.

Complexities arise because the nanoparticle aggregates, while fractal-like, are not truly scale-invariant structures. They consist of finite-size particles, and possess many other characteristic length scales as well. Extracting the fractal dimensions from such complex systems with cryo-tomography is not trivial. As discussed, finite volume effects must be carefully accounted for, and multiple sample volumes should be considered for statistical reliability. With this system, the fractal power-law behavior was only quantifiable over a limited range (approximately 5−50 nm).

Aggregate Structure. Cryo-tomography clearly shows that ferrihydrite particle suspensions may aggregate to form branched aggregate structures. These appear to be fractal-like with low intrinsic fractal dimensions.

The level of structural diversity within a given sample and between samples is notable, but the physical cause for the difference between Syn10 and Syn15 is unknown. One possibility we initially considered is aging time: Syn10 was

prepared first, and it was possible that Syn15 would, upon aging, resemble Syn10. However, our subsequent time series data for Syn15 do not support this hypothesis. After aging for up to 8 months, the basic aggregate structure of Syn15 seems to remain stable; only average aggregate size appears to increase. Thermal treatment of Syn15 also caused very little quantifiable change in aggregate structure. Instead, it seems that Syn10 and Syn15 were set on different aggregation trajectories very early in the aggregation process, perhaps due to a subtle variation in solution chemistry or due to features inherited from synthesis such as detailed particle morphology. The exact cause for the structural differences between our syntheses remains unknown, and subsequent experiments using this synthesis have shown an even greater range of aggregate structures than reported here. Although our study was not designed to determine aggregation mechanism, one possible cause for the variation involves subtle differences in pH during synthesis, as recent work by Yuwono[32] has shown that aggregation in related ferrihydrite systems may be altered by small changes in pH, even at conditions well below the point of zero net proton charge where it was previously assumed that pH would have minimal influence on aggregation behavior.

The structures of both Syn10 and Syn15 differ significantly from those predicted by traditional models of aggregation. The commonly assumed DLCA mechanism, in which fractal structures arise to due stochastic collisions between clusters and hard spheres, is expected to produce aggregate fractal dimensions between 1.6 and 1.9.[28] Of course, DLCA is expected to be rapid and is unlikely to control the development of aggregates which grow slowly over the course of months, as was observed for Syn15. In these cases, an RLCA mechanism is more likely to apply. Simple models for RLCA generally predict the formation of more densely packed aggregates, with fractal dimension of greater than 2. These types of values have been observed in calcium phosphate nanostructures.[8] However, the low dimension of the branched fractal aggregates seen in this study are not fully explained by either the DLCA- or the RLCA-based mechanism. It seems that a more complex particle interaction must be present here, which not only reduces the probability for particle attachment (as in RLCA) but also preferentially selects for certain attachment positions and stabilizes the formation of linear particle chains.

The aggregate structures may be influenced by "long"-distance interparticle forces, such as those predicted by DLVO theory for electrostatic repulsion in a dilute electrolyte solution. These forces typically extend for tens of nanometers. Over the length scales probed, these may limit the trajectories for particle attachment and/or stabilize the aggregates against collapse. If this is the case, such low-dimension structures may be typical for nanoparticle aggregates. Alternatively, short-range crystallographically direction-specific interactions could favor the formation of nanoparticle chains. Such oriented aggregation effects have been known to lead to crystal growth under some conditions.[19] The formation of single-crystal laths in Syn10 (which also has very linear chains) seems to support this later hypothesis. In any case, if the low fractal dimension is controlled by relatively local interactions, very large aggregates are likely to possess more traditional aggregate morphologies when observed on macroscopic length scales.

The low observed fractal dimensions have directly observable physical consequences. Historically, local aggregate structure was not directly observable, and fractal geometries have provided a useful tool for modeling the local branching structure, so that physical properties can be estimated. Fractal structure has been correlated with aggregate mechanical strength, hydrodynamic behavior, transport, and persistence in the environment.[13] For example, aggregates with low fractal dimension are less susceptible to gravitational settling.[12] Thus, the low fractal dimension seen here explains how ferrihydrite suspensions can be extensively aggregated yet remain stable against sedimentation. It can also be shown that the lower fractal dimensions lead to suspensions that are more optically transparent. In the future, direct measurement of aggregate structures may provide a method for direct computation of these properties.

■ CONCLUSION

The tomographic methods described in this work have been used to directly determine the three-dimensional structure of fragile, nanoparticle aggregates *in aqua*. This has allowed a direct estimation of the fractal dimension of these aggregates. On length scales up 100 nm, the aggregates are dominated by linear structures, characterized by low fractal dimension. These structures are not predicted by traditional models of stochastic colloidal aggregation. This finding should have important ramifications for nanoparticle behavior, since fractal dimension can impact aggregate stability, flocculation rates, and transport behavior.

Our work demonstrates the challenges involved with determining meaningful fractal dimensions from suspensions of complex, polydisperse nanoparticle aggregates. In such systems, SAXS-based methods are not sufficient to fully determine the aggregate structure. The introduction of cryo-tomography provides an alternative method for determining fractal dimension in these cases. The determination of fractal dimension from tomographic data sets presents its own challenges, especially regarding the proper treatment of finite-size effects and the acquisition of adequate statistics, but it should prove invaluable for exploring the structure of complex and highly polydisperse aggregate suspensions whose characterization by SAXS alone would be intractable.

■ ASSOCIATED CONTENT

Ⓢ Supporting Information

Text describing additional information on the SI figures and notes on SAXS fitting, figures showing autocorrelation functions, tomograms from Syn10, projection views of computationally generated DLA-based aggregate containing 100,000 particles and 3D volumes extracted from the center of a given aggregate, and video showing 360° rotational view of four selected aggregates. This material is available free of charge via the Internet at http://pubs.acs.org.

■ AUTHOR INFORMATION

Present Addresses

∥Pacific Northwest National Laboratory, Richland, WA 99352. ⊥Ecosystem Science and Management, University of Wyoming, Laramie, WY, 82071.

Notes

The authors declare no competing financial interest.

■ ACKNOWLEDGMENTS

■ REFERENCES

(1) Liu, J.; Aruguete, D. M.; Murayama, M.; Hochella, M. F. Influence of Size and Aggregation on the Reactivity of an Environmentally and Industrially Relevant Nanomaterial (PbS). *Environ. Sci. Technol.* **2009**, *43*, 8178−8183.

(2) Dunphy Guzman, K. A.; Finnegan, M. P.; Banfield, J. F. Influence of Surface Potential on Aggregation and Transport of Titania Nanoparticles. *Environ. Sci. Technol.* **2006**, *40*, 7688−7693.

(3) Gilbert, B.; Ono, R. K.; Ching, K. A.; Kim, C. S. The Effects of Nanoparticle Aggregation Processes on Aggregate Structure and Metal Uptake. *J. Colloid Interface Sci.* **2009**, *339*, 285−295.

(4) Adrian, M.; Dubochet, J.; Lepault, J.; McDowall, A. W. Cryo-electron Microscopy of Viruses. *Nature* **1984**, *308*, 32−36.

(5) Pouget, E. M.; Bomans, P. H. H.; Goos, J. A. C. M.; Frederik, P. M.; de With, G.; Sommerdijk, N. A. J. M. The Initial Stages of Template-Controlled CaCO$_3$ Formation Revealed by Cryo-TEM. *Science* **2009**, *323*, 1455−1458.

(6) Yuwono, V. M.; Burrows, N. D.; Soltis, J. A.; Penn, R. L. Oriented Aggregation: Formation and Transformation of Mesocrystal Intermediates Revealed. *J. Am. Chem. Soc.* **2010**, *132*, 2163−2165.

(7) Midgley, P. A.; Dunin-Borkowski, R. E. Electron Tomography and Holography in Materials Science. *Nat. Mater.* **2009**, *8*, 271−280.

(8) Habraken, W. J. E. M.; et al. Ion-association Complexes Unite Classical and Non-classical Theories for the Biometic Nucleation of Calcium Phosphate. *Nature Commun.* **2013**, *4*, No. 1507, DOI: 10.1038/ncomms2490.

(9) Frandsen, C. A.; Legg, B. A.; Comolli, L. R.; Zhang, H.; Gilbert, B.; Johnson, E.; Banfield, J. F. Aggregation-Induced Growth and Transformation of β-FeOOH Nanorods to Micron-Sized α-Fe$_2$O$_3$ Spindles. *CrystEngComm* **2014**, *16*, 1451−1458.

(10) Gilbert, B.; Lu, G.; Kim, C. S. Stable Cluster Formation in Aqueous Suspensions of Iron Oxyhydroxide Nanoparticles. *J. Colloid Interface Sci.* **2007**, *313*, 152−159.

(11) Guyodo, Y.; Mostrom, A.; Lee Penn, R.; Banerjee, S. K. From Nanodots to Nanorods: Oriented Aggregation and Magnetic Evolution of Nanocrystalline Goethite. *Geophys. Res. Lett.* **2003**, *30*, 1512-1−1512-4.

(12) Gmachowski, L. Aggregate Structure and Hydrodynamics of Aggregated Systems. *Colloids Surf., A* **2005**, *255*, 105−110.

(13) Manley, S.; Cipelletti, L.; Trappe, V.; Bailey, A. E.; Christianson, R. J.; Gasser, U.; Prasad, V.; Segre, P. N.; Doherty, M. P.; Sankaran, S.; Jankovsky, A. L.; Shiley, B.; Bowen, J.; Eggers, J.; Kurta, C.; Lorik, T.; Weitz, D. A. Limits to Gelation in Colloidal Aggregation. *Phys. Rev. Lett.* **2004**, *93*, No. 108302.

(14) Meakin, P. Aggregation Kinetics. *Phys. Scr.* **1992**, *46*, 295−331.

(15) Kremer, J. R.; Mastronarde, D. N.; McIntosh, J. R. Computer Visualization of Three-Dimensional Image Data Using IMOD. *J. Struct. Biol.* **1996**, *116*, 71−76.

(16) Agulleiro, J. I.; Fernandez, J. J. Fast Tomographic Reconstruction on Multicore Computers. *Bioinformatics* **2011**, *27*, 582−583.

(17) Kaynig, V.; Fuchs, T.; Buhmann, J. M. Neuron Geometry Extraction by Perceptual Grouping in ssTEM Images. *2010 IEEE Conference on Computer Vision and Pattern Recognition (CVPR)*; IEEE Computer Society: Washington, DC, USA, 201029022909

(18) Ilavsky, J.; Jemian, P. R. *Irena*: Tool Suite for Modeling and Analysis of Small-Angle Scattering. *J. Appl. Crystallogr.* **2009**, *42*, 347−353.

(19) Burleson, D. J.; Penn, R. L. Two-Step Growth of Goethite from Ferrihydrite. *Langmuir* **2006**, *22*, 402−409.

(20) Teixeira, J. Small-Angle Scattering by Fractal Systems. *J. Appl. Crystallogr.* **1988**, *21*, 781−785.

(21) Gmachowski, L. Calculation of the Fractal Dimension of Aggregates. *Colloids Surf., A* **2002**, *211*, 197−203.

(22) Bushell, G. C.; Yan, Y. D.; Woodfield, D.; Raper, J.; Amal, R. On Techniques for the Measurement of the Mass Fractal Dimension of Aggregates. *Adv. Colloid Interface Sci.* **2002**, *95*, 1−50.

(23) Sinha, S. K. Scattering from Fractal Structures. *Physica D* **1989**, *38*, 310−314.

(24) Meakin, P. Formation of Fractal Clusters and Networks by Irreversible Diffusion-Limited Aggregation. *Phys. Rev. Lett.* **1983**, *51*, 1119−1122.

(25) Dimon, P.; Sinha, S. K.; Weitz, D. A.; Safinya, C. R.; Smith, G. S.; Varady, W. A.; Lindsay, H. M. Structure of Aggregated Gold Colloids. *Phys. Rev. Lett.* **1986**, *57*, 595−598.

(26) Porod, G. In *Small Angle X-Ray Scattering*; Glatter, O., Kratky, O., Eds.; Academic Press: London, 1982; pp 18−59.

(27) Nicolai, T.; Durand, D.; Gimel, J.-C. Static Structure Factor of Dilute Solutions of Polydisperse Fractal Aggregates. *Phys. Rev. B* **1994**, *50*, 16357−16363.

(28) Sposito, G. Scaling Invariance of the von Smoluchowski Rate Law. *Colloids Surf., A* **1997**, *120*, 101−110.

(29) Lin, M. .; Klein, R.; Lindsay, H. .; Weitz, D. .; Ball, R. .; Meakin, P. The Structure of Fractal Colloidal Aggregates of Finite Extent. *Colloids Surf., A* **1990**, *137*, 263−280.

(30) Yanwei, Z.; Meriani, S. Scaling Functions for the Finite-Size Effect in Fractal Aggregates. *J. Appl. Crystallogr.* **1994**, *27*, 782−790.

(31) Oliphant, T. E. Python for Scientific Computing. *Comput. Sci. Eng.* **2007**, *9*, 10−20.

(32) Yuwono, V.M.; Burrows, N.D.; Soltis, J.A.; Do, T.A.; Penn, R.L. Aggregation of ferrihydrite nanoparticles in aqueous systems. *Faraday Discuss.* **2012**, *159*, 235−245.

(33) Kline, S. R. Reduction and Analysis of SANS and USANS Data using Igor Pro. *J. Appl. Crystallogr.* **2006**, *39*, 895.